

Review

# Radiofrequency Coils for Low-Field (0.18–0.55 T) Magnetic Resonance Scanners: Experience from a Research Lab–Manufacturing Companies Cooperation

Giulio Giovannetti <sup>1,\*</sup> , Francesca Frijia <sup>2</sup> and Alessandra Flori <sup>2</sup> <sup>1</sup> Institute of Clinical Physiology, National Council of Research, 56124 Pisa, Italy<sup>2</sup> U.O.C Bioengineering and Clinical Technology, Fondazione G. Monasterio CNR—Regione Toscana, 56124 Pisa, Italy

\* Correspondence: giovannetti@ifc.cnr.it; Tel.: +39-050-3152794

**Abstract:** Low-field magnetic resonance imaging (MRI) has become increasingly popular due to cost reduction, artifact minimization, use for interventional radiology, and a better safety profile. The different applications of low-field systems are particularly wide (muscle–skeletal, cardiac, neuro, small animals, food science, as a hybrid scanner for hyperthermia, in interventional radiology and in radiotherapy). The low-field scanners produce lower signal-to-noise ratio (SNR) images with respect to medium- and high-field scanners. Thus, particular attention must be paid in the minimization of the radiofrequency (RF) coil losses compared to the sample noise. Following a short description of the coil design and simulation methods (magnetostatic and full-wave), in this paper we will describe how the choice of electrical parameters (such as conductor geometry and capacitor quality) affects the coil's overall performance in terms of the quality factor  $Q$ , ratio between unloaded and loaded  $Q$ , and coil sensitivity. Subsequently, we will summarize the work carried out at our electromagnetic laboratory in collaboration with MR-manufacturing companies in the field of RF coil design, building, and testing for 0.18–0.55 T magnetic resonance (MR) clinical scanners by classifying them between surface-, volume-, and phased-array coils.

**Keywords:** magnetic resonance imaging; low-field MRI; RF coils

**Citation:** Giovannetti, G.; Frijia, F.; Flori, A. Radiofrequency Coils for Low-Field (0.18–0.55 T) Magnetic Resonance Scanners: Experience from a Research Lab–Manufacturing Companies Cooperation. *Electronics* **2022**, *11*, 4233. <https://doi.org/10.3390/electronics11244233>

Academic Editor: Yu Zhang

Received: 24 November 2022

Accepted: 15 December 2022

Published: 19 December 2022

**Publisher's Note:** MDPI stays neutral with regard to jurisdictional claims in published maps and institutional affiliations.



**Copyright:** © 2022 by the authors. Licensee MDPI, Basel, Switzerland. This article is an open access article distributed under the terms and conditions of the Creative Commons Attribution (CC BY) license (<https://creativecommons.org/licenses/by/4.0/>).

## 1. Introduction

Magnetic resonance imaging (MRI) is among the most important non-invasive and non-ionizing medical imaging techniques for the diagnosis and follow-up of diseases which affect different organs and tissues. The great increase in availability of MRI scanners in the last three decades has permitted access to this technology for many radiology departments, even in small hospitals and clinics.

Although the 1.5 T MR scanner has become the standard clinical system even in small health care facilities, and despite the increase in the installation of whole-body 7 T systems (mainly for clinical research studies), in recent years the magnetic resonance (MR) community has shown an increasing interest towards low-field scanners.

Low-field MRI provides several advantages compared to medium- and high-field MRI, such as a more convenient and cheaper setting, reduced operating and maintenance costs, greater patient comfort, and a better safety profile. In MRI studies, the signal-to-noise ratio (SNR) and the spatial resolution generally increase with the magnetic field strength. Therefore, low-field MRI scanners produce images with a lower SNR and spatial resolution when compared to high-field body scanners. However, the worse image quality does not necessarily reduce diagnostic accuracy in many applications (such as muscle–skeletal, cardiac, and neurological) and low-field MRI systems are increasingly involved in a wide range of clinical and research studies, including the use of hybrid scanners for

hyperthermia, interventional radiology, and radiotherapy, and even in small animal studies and food science [1,2].

MRI makes use of a strong static magnetic field coupled with radiofrequency (RF) pulses and gradients for image acquisition. The RF field is generated by the transmit coil and excites the protons within biological tissues, after which the re-emitted signal is picked up by a receive coil. Among several other factors, the performance of the RF coils employed for image acquisition plays a key role in image quality, especially in low-field scanners where particular attention must be paid to the minimization of the RF-coil losses with respect to the sample noise [3].

There are three main types of low-field strength MRI: resistive magnets, permanent magnets, and superconducting magnets. The resistive magnets are light and generate a high field uniformity but have high energy consumption. However, they only require simple water cooling without the use of expensive cryogenics. The permanent magnets do not require power for generating the magnetic field—only electronics and gradients need power—and are therefore considered highly energy efficient [4,5]. The development of superconductive magnets made significantly higher field strengths possible (typically > 0.5 T), but they require additional high-power facilities and a quench pipe for cryogenic cooling [2]. The more common, basic geometry of the permanent magnet is a C-shape, which determines the vertical orientation of the  $B_0$  static field. In this configuration, the high-efficiency coil is a solenoid placed around the head of the thorax with its main axis aligned along the body length [1]. With the constraint that its axis must be positioned perpendicular to the main magnetic-field orientation, a loop coil can be optimally positioned around the body part being imaged for different organ regions. In the case of tunnel-type resistive or superconductive magnets, the magnetic field ( $B_0$ ) orientation is along the longitudinal patient axis, and they are ideally suited for the use of multichannel array coils [6].

In this paper, we initially provide a short description of the simulation methods which are generally employed for low-field coil design according to two different approaches (magnetostatic and full-wave). Subsequently, we describe how the coils' overall performance (quality factor  $Q$ , ratio between unloaded and loaded  $Q$ , and coil sensitivity) is affected by the choice of electrical parameters (the coil conductor geometry and capacitor quality). Finally, we summarize the work carried out in our research institute's electromagnetic laboratory, which was performed in collaboration with some MR manufacturing companies in the field of RF coil design, simulation, building, and testing for 0.18–0.55 T MR clinical scanners by classifying them according to coil geometry (surface-, volume-, and phased-array).

## 2. Methods for Coils Design and Simulation

### 2.1. Magnetostatic Theory

Magnetostatic theory relies on the nearly static field assumption, which is verified only when the coil sizes are much lower ( $<1/10$ ) than the wavelength. The estimation of the magnetic field generated by the currents along the coil conductors can be calculated by subdividing the coil path into segments to separately evaluate their total field contribution.

The magnetic field produced by a steady electric current  $I$  flowing in an arbitrary closed contour  $C$  can be calculated by using the Biot–Savart law:

$$B(r) = \frac{\mu_0 I}{4\pi} \int_C \frac{dl \times R}{R^3} \quad (1)$$

where  $\mu_0 = 4\pi \times 10^{-7}$  (H/m) is the free space permeability,  $dl$  is the infinitesimal vector tangential to  $C$ , and  $R$  is the distance between the observation point and the conductor path [7].

The Biot–Savart equation can be used for simulating the  $B_1$  RF field distributions of coils constituted of linear and circular conductor segments. When using such an equation, the conductor size is neglected when compared to the wavelength and the generated magnetic field is evaluated by replacing the conductors with very thin wires. Figure 1 shows an example of the magnetostatic simulation of a 5 cm radius circular coil lying on the

x,y plane and centered at x = 0 and y = 0. In particular, Figure 1a refers to the magnetic-field pattern calculated at a z-coordinate of 2 cm, while Figure 1b shows the profile plot (along the z-axis) of the magnetic-field pattern as a function of the depth profile.

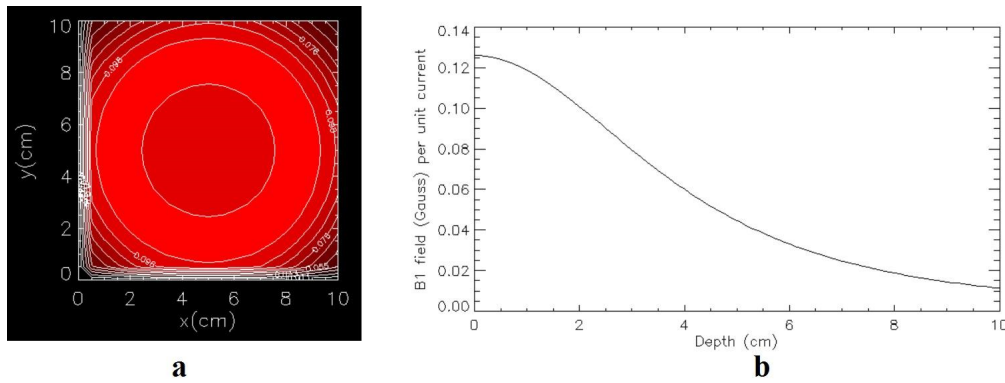


**Figure 1.** A 5 cm radius circular coil magnetostatic simulation: (a) the normalized magnetic field as a contour plot at z = 2 cm and (b) the normalized magnetic field in the z-axis vs. the depth profile.

In the magnetostatic approach, the inductance  $L$  of a conductor can be calculated by using the following expression:

$$L = \frac{\mu_0}{4\pi I^2} \iiint_V \iiint_V \frac{J(r) \cdot J(r')}{R} d\mathbf{v}d\mathbf{v}' \tag{2}$$

where  $J$  is the current density in the conductor,  $I$  represents the total current in the conductor,  $V$  is the conductor volume, and  $R = r - r' \nabla$  [7].

For example, the inductance calculation for a loop of radius  $b$ , constituted by a strip with width  $w$ , can be carried out using the following expression [8]:

$$L_{\text{strip}} = \frac{\mu_0}{4\pi w^2} \int_{-w/2}^{w/2} \int_0^{2\pi} \int_{-w/2}^{w/2} \int_0^{2\pi} \frac{\cos(\theta' - \theta)(b+r)(b+r')}{R} d\theta dr d\theta' dr' \tag{3}$$

where

$$R = \sqrt{[(b+r) \cos \theta - (b+r') \cos \theta']^2 + [(b+r) \sin \theta - (b+r') \sin \theta']^2} \tag{4}$$

Figure 2 shows a segment of the circular coil strip conductor.

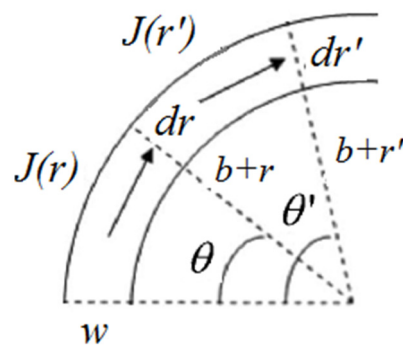


**Figure 2.** A circular coil strip conductor segment.

### 2.2. Full-Wave Methods

At increasing magnetic-field strengths, the nearly static field assumption is no longer satisfied, and the magnetostatic theory cannot be employed for coil design. However, even at low frequencies, developing a sample-coil interaction model can be useful for designing

a system strictly coupled to the sample in order to minimize the coil noise with respect to the sample noise.

Full-wave methods have been largely employed for this purpose, with the great advantage that they permit designing coils that have a complex shape and that are loaded with models of the body exposed.

Such full-wave methods can be classified according to whether the computation is performed in the time or frequency domain and if the method is based on integral or differential equations. The more widely used full-wave methods for the design and simulation of coils are the finite element method (FEM), the method of moments (MoM), and the finite-difference time-domain method (FDTD) [9].

The FEM is a differential equation approach based on the discretization of the mesh elements of the entire computational domain, including the surrounding environment. FEM divides the region of interest into irregular cells, usually tetrahedral elements, which accurately model arbitrary geometries. The field equations are written by means of polynomials with unknown coefficients defined on the mesh nodes or along element edges. The differential equations and the associated boundary conditions are then converted into an integro-differential formulation by minimizing a function or using a weighted residual method. By applying this integro-differential formulation to a single element with suitable weights and interpolation functions, a series of equations is obtained for each element and for the entire computational domain. A global matrix system is then produced and solved by inversion or iterative techniques in the frequency domain [10]. The FEM is largely used in science and engineering applications due to its high geometrical modeling ability. However, if it is used for an RF coil loaded with an accurate human model, the matrix equation dimension can be very large.

The MoM is also based on the resolution of integral equations in the frequency domain. In particular, an integro-differential equation is first formulated in terms of equivalent current, taking into account the permittivity and conductivity effects of an inhomogeneous sample. This equation is subsequently discretized using Galerkin's method to obtain a matrix equation whose solution provides the numerical solution of the problem. The electromagnetic problem is then reduced to the solution of a system of linear equations for which suitable basis functions in each geometric element of the discretization mesh are chosen:

$$[Z][I] = [V] \quad (5)$$

where the impedance matrix  $[Z]$  represents the lumped elements,  $[I]$  is the current vector to be determined, and  $[V]$  is the voltage vector (including the excitation source) [11]. MoM is very efficient when dealing with perfectly conducting sources and homogeneous media, while the computational load can be significantly higher for coil and sample simulations.

The FDTD method solves Maxwell's equations in the time domain using a discretization of the spatial and temporal parameters with the finite difference approximation. To solve the equation for the electrical and magnetic fields, the sample must be enclosed in a box and the computational domain is divided into cubic cells (Yee's cells). The components of the electric field are assigned at the center of each cell's edge, while the components of the magnetic field are assigned at the center of each cell's face. Starting from the initial values of the electric and magnetic field and, with a specific excitation, the process iteratively calculates the field values of each cell using a central finite difference approximation for resolving spatial and temporal derivatives in Maxwell's equations. The electric field is updated using its value in the previous step and the value of the magnetic field at the intermediate step. Similarly, the magnetic field updates, beginning from the magnetic field obtained to the previous step and the electric field obtained in the intermediate step [12]. In order to achieve a highly accurate mesh truncation, it is necessary to choose optimal boundary conditions. In the research activities described in this paper, the perfectly matched layer (PML) condition was employed. The PML condition is an artificial absorber type, useful for annihilating the outgoing fields originating from the computational domain in order to minimize the reflection from the truncation boundary. The computational domain

boundary condition (cells to simulation area), which is the distance between the PML and simulated objects, was set to 20. The PML number for all low-frequency simulations was also set to 20. In conclusion, the FDTD method is currently the most commonly employed method for obtaining high-resolution electromagnetic-field-distribution maps in numerical field calculations considering realistic, human electromagnetic body models, since it does not require solving any matrix equations.

### 3. Coil Performance Evaluation

#### 3.1. Quality Parameters

The coil quality factor  $Q$  can be calculated as [7]:

$$Q = \frac{2\pi f_0 L}{R_{tot}} = \frac{1}{R_{tot}} \sqrt{\frac{L}{C}} \quad (6)$$

where the inductance  $L$  stands for the energy stored in the magnetic field, the capacitance  $C$  mainly takes into account the discrete capacitor's contribution, and the resistance  $R_{tot}$  represents the total losses in the coil:

$$R_{tot} = R_{coil} + R_{sample} \quad (7)$$

where  $R_{coil}$  takes into account the losses within the receiver coil conductors and the lumped element losses and  $R_{sample}$  represents the sample-induced losses caused by RF currents and electric fields in the sample.

The coil performance can also be characterized by the ratio  $r$  between the quality factor of the empty resonator ( $Q_{unloaded}$ ) and of the resonator in the presence of the sample ( $Q_{loaded}$ ) as in [13]:

$$r = \frac{Q_{unloaded}}{Q_{loaded}} = 1 + \frac{R_{sample}}{R_{coil}} \quad (8)$$

Another parameter describing the coil performance is the efficiency, defined as the ratio between the intensity of the magnetic field  $B_1$  at a given point in space and the supplied power  $P$  [14]:

$$\eta = \frac{B_1}{\sqrt{P}} \quad (9)$$

The reciprocity theorem [15] allows the use of Equation (9) for characterizing both the transmit and receive performance of a coil.

#### 3.2. SNR Evaluation

The signal-to-noise ratio (SNR) is an accepted standard for quality assessment in MRI and is dependent on several factors, including the hardware (particularly the main field strength and RF coils), the acquisition sequence parameters, and the tissue relaxation properties. It can be calculated as the ratio between the induced RF signal and the root-mean-square (RMS) of the thermal noise voltage measured at the coil terminals [16]:

$$SNR_P = \frac{2\pi f_0 M V B_P}{\sqrt{4kT \Delta f R_{tot}}} \quad (10)$$

where  $f_0$  is the Larmor frequency,  $M$  is the magnetization,  $V$  is the voxel volume,  $B_P$  is the receiver coil magnetic field per unit current at the observation point  $P$ ,  $k$  is the Boltzmann constant,  $T$  is the absolute resistance temperature, and  $\Delta f$  is the receiver bandwidth.

The frequency dependence of the SNR can be analyzed by taking into account the different contributions of the losses as a function of the frequency  $f$  and by considering a sample of linear size  $d$ . In particular, by taking into account the current distribution in the coil conductor's cross-section, in which  $R_{coil} \approx f^{\frac{1}{2}} d^{-1}$ , whereas in the near-field assumption  $R_{sample} \approx f^2 d^3$  [17]. We can assume that, at low RF frequencies, the SNR is

mainly determined by the coil losses and  $SNR \approx f^{\frac{7}{4}} d^2$  [3]. In this regime, the SNR can be increased by using coils with a high Q factor, since for a coil tuned at  $f_0$  the  $SNR \approx \sqrt{Q}$  [18]. Conversely, at high RF frequencies the sample losses dominate and  $SNR \approx f d^{\frac{1}{2}}$ . This is what generally occurs at clinical fields (>0.5 T) [19]. However, for low-frequency coils strictly coupled to the sample, the contributions from coil noise and sample noise could be approximately equal and even a sample-induced resistance estimation has to be taken into account for SNR estimation.

In summary, in order to increase the image quality for low-field MRI scanners, generally a careful coil design has to be taken into account. In particular, the choice of the cross-geometry and the quality factor of the conductors affects the overall performance of the coil.

## 4. Optimal Low-Field Coils Design

### 4.1. Conductors

An alternating current (AC) which flows in a conductor is not uniformly distributed across its section, but its density decreases exponentially with the distance from the boundary surface. For an AC resistance estimation, the current is considered confined in a region near the surface whose thickness is given by the penetration depth [20]:

$$\delta = \sqrt{\frac{\rho}{\pi f \mu_0}} \quad (11)$$

where  $\rho$  is the conductor resistivity ( $1.68 \cdot 10^{-8} \Omega \cdot \text{m}$  for copper) and  $f$  is the coil tuning frequency. Consequently, the conductor volume crossed by the RF current is limited by the value of the penetration depth, giving the so-called “classical skin effect” [21]. However, the tendency of the current density to concentrate toward the surface is more pronounced at the points with the greatest curvature (i.e., at the conductor edges). This phenomenon is called the “lateral skin effect” [22] and, in this case, the coil resistance is given by the sum of the lateral and the classical skin effect resistances [23].

RF coils are generally built using conductors with two different cross-sectional geometries, i.e., circular wire and flat strip (hereafter named “wire” and “strip”, respectively). Due to the lateral skin effect, the current distribution in the strip is less uniform than in the wire. As has been suggested in the literature, the strip thickness should be at least six times the skin depth for maximizing the surface where the current flows and therefore minimizing the conductor resistance at the frequency used [24].

Giovannetti et al. [25] compared low-frequency birdcage coils with the same dimensions and resonant frequency (7.66 MHz, which was the  $^1\text{H}$  frequency for 0.18 T magnetic field and corresponded to a penetration depth of 23  $\mu\text{m}$ ): two of them were constituted by strip conductors of a 1 cm width with different thickness (35 and 800  $\mu\text{m}$ , the latter much higher than the penetration depth at the working frequency), and a third was built using a 4.5 mm diameter wire conductor with the same conductor inductance.

A workbench test performed with the different birdcages in terms of Q factor,  $r$  ratio between unloaded and loaded (with a saline solution phantom) Q, and coil sensitivity showed that the use of strips with a thickness much higher than the penetration depth led to increased overall coil performance, thanks to the decrease in conductor resistance.

However, the use of the wire conductor led to improved performance with an increase of 28% in the Q, 26% in the  $r$  ratio, and 22% in sensitivity with respect to the best strip-based coil.

A comparison between two circular loops with a 7.5 cm radius, built using a strip and a wire conductor and having the same inductance value, underlined the better performance of the wire. In particular, the workbench tests performed on the two coils tuned at 5.7 MHz showed that the wire coil provided an increase of 59% in the Q factor with respect to the strip coil [26].

## 4.2. Capacitors

The quality factor of a capacitor with capacitance  $C$  represents its efficiency in terms of energy losses and is defined as [14]:

$$Q_c = \frac{1}{2\pi f_0 C ESR} \quad (12)$$

where  $f_0$  is the measurement frequency and  $ESR$  is the equivalent series resistance representing the conductor resistance and dielectric losses effects. While  $Q_c$  values of commercial capacitors are typically quoted in the several hundreds, fixed and variable capacitors for coil tuning and matching are specially designed in a non-magnetic version with a high-quality factor and high breakdown voltage.

Giovannetti et al. [27] reported a comparison between commercial and high-quality capacitors employed on two 5.25 cm radius circular coils tuned at 21.29 MHz, close to the  $^1\text{H}$  frequency at 0.5 T. One coil was tuned with commercial capacitors ( $Q_c > 500$  at unspecified frequencies), while the second was tuned using high-quality capacitors ( $Q_c > 10.000$  at 1 MHz). Both coils were tested with an HP 3577A (Hewlett Packard, Palo Alto, CA) network analyzer and a dual-loop probe. The test consisted of measuring the unloaded and loaded  $Q$  by using a homogeneous, cubic sample filled with saline solution (2.4 g/L NaCl). Results underlined that the use of high- $Q$  capacitors led to a significant increase in coil performance, providing a doubled  $r$  factor and an unloaded  $Q$  factor that increased from 15 to 399. Such outcomes demonstrated that high-quality capacitors are necessary for obtaining high-performance coils working at a low frequency. In another paper, two low-pass birdcage-coil prototypes with identical dimensions (11 cm height and 14 cm diameter) were designed and tuned at the same resonant frequency (7.66 MHz, corresponding to a proton frequency of 0.18 T) by using commercially available ceramics capacitors (with a low quality factor) and high-quality capacitors ( $Q_c > 10.000$  at 1 MHz) developed by ATC, respectively [25]. Workbench tests were performed with a load consisting of a cylindrical, homogeneous phantom of saline solution simulating the knee conductivity and constituting 55 mM of NaCl and 5 mM of  $\text{NiCl}_2$ . Results showed that the coil employing standard-quality capacitors provided very low performance ( $Q = 21$  and  $r = 1.04$ ), while performance strongly increased using the high-quality capacitors supplied by ATC ( $Q = 228$  and  $r = 2.05$ ). The coil sensitivity, measured with the perturbing sphere method, increased from 11.92 to 34.61  $\mu\text{T}/\text{w}^{1/2}$ .

## 5. Low-Field Coils

### 5.1. Surface Coils

Circular and square geometries are the simplest designs for a single surface coil. They both produce a  $B_1$  field perpendicular to the coil plane in the central region of the coil, with an amplitude that decreases along the coil axis.

Giovannetti et al. [28] described the development of a coil-SNR model based on the theory of equivalent electric circuits and its application to a circular- and square-loop design tuned at different frequencies, including 21 MHz (e.g., the proton frequency at 0.5 T).

In this study, the coil resistance was estimated using Ohm's law as a function of the geometry of the coil conductor path. The magnetic-field pattern was calculated in parallel using magnetostatic analysis and the sample-induced resistance was calculated using a method employing vector-potential calculation, which can be easily mathematically implemented and is characterized by a short computation time [29]. Finally, the integral method was used to calculate the conductor inductance. Coil-losses estimation was completed with the addition of the capacitor losses, obtained from the capacitor datasheet, and the resistive losses of solder joints (extrapolated from the literature data), which were 18 and 10 m $\Omega$  at 21 MHz, respectively.

Theoretical considerations suggest that when a simple relationship between a circular loop of radius  $b$  and a square loop of side  $S$  is satisfied the resultant performance of both coils is very similar in terms of the  $r$  parameter and consequently the SNR.

However, in a real MR experiment, the coil shape can be very different with respect to circular and square loops, especially when particular fields-of-view (FOVs) are desired.

Giovannetti et al. [30] proposed an FDTD-based procedure for estimating the sample-induced resistance of different 10.5 MHz-tuned saddle coils with variable straight conductor dimensions and loaded with a cylindrical sample whose dielectric properties meet the American Society for Testing and Material (ASTM) criteria used to develop MR phantoms ( $\epsilon_r = 80$ ,  $\sigma = 0.6$  S/m) [31]. The employed full-wave tool was the general electromagnetic simulator (GEMS), a three-dimensional, high-performance, parallel FDTD simulation package. The coils were designed for the spine imaging of big dogs. After the magnetic-field patterns were calculated using magnetostatic theory, the sample-induced resistance was estimated by calculating the  $Q$ , circuit quality factor after a perturbing Gaussian pulse and by measuring the energy losses during the voltage damping across a coil capacitor. Such an algorithm allowed for the search for the coil's maximum-sensitivity value in dependence on the sample size and geometry. Moreover, the coil curvature was chosen to account for such big animals while guaranteeing a wide FOV with good penetration in deep sample regions. Simulation results were validated on two saddle-coil prototypes. The experimental tests consisted of the evaluation of unloaded and loaded coil quality factors using a cylindrical, homogeneous phantom of saline solution (2 L of 55 mM NaCl and 5 mM NiCl<sub>2</sub>) as biological sample and provided a deviation lower than 5% with respect to simulation. Although there are technical difficulties involved in coil and cryostat design, a substantial SNR improvement can be achieved by using high-temperature superconducting (HTS) RF-receive-surface coils, as are employed for human and phantom image acquisitions with a 0.2-T scanner. In particular, SNR gains of 2.8-fold and 1.4-fold were measured in phantom images acquired with an HTS coil versus a room-temperature copper coil and a liquid-nitrogen-cooled copper coil, respectively [32].

## 5.2. Volume Coils

Birdcage coils are extensively used in MRI as transmitter and receiver coils and are characterized by more than one resonant mode: an  $N$ -leg coil will supply  $N/2+2$  distinct resonant modes, although the working resonant mode in MRI is the fundamental one [33].

Giovannetti et al. [34] described a high-pass and low-pass birdcage-coil simulator employing the magnetostatic theory for a high-accuracy estimation of the complete resonant frequency spectrum of the coil and of the relevant magnetic field pattern, which depends on the coil dimensions and the number of legs [18]. In particular, the simulator—based on the method of the equivalent circuit and developed using the Interactive Data Language (IDL 6.0 Visual Information Solutions, Boulder, CO, USA) environment—accounted for the mutual inductances and the effect of a radiofrequency shield for birdcages composed of strip or wire conductors. The simulator accuracy was validated by developing and testing a low-pass birdcage coil (with a 12 cm length and 13.4 cm diameter) tuned at 8 MHz. Figure 3 shows the simulated magnetic field pattern of such a coil, referred to as the fundamental mode (mode 1). The comparison between the theoretical and measured values of the resonant frequencies showed a deviation lower than 2.2% and 4.2% for the unshielded and shielded coils, respectively. Moreover, the proposed birdcage coil provided a good magnetic field uniformity measured in the central transverse plane perpendicular to the coil axis.

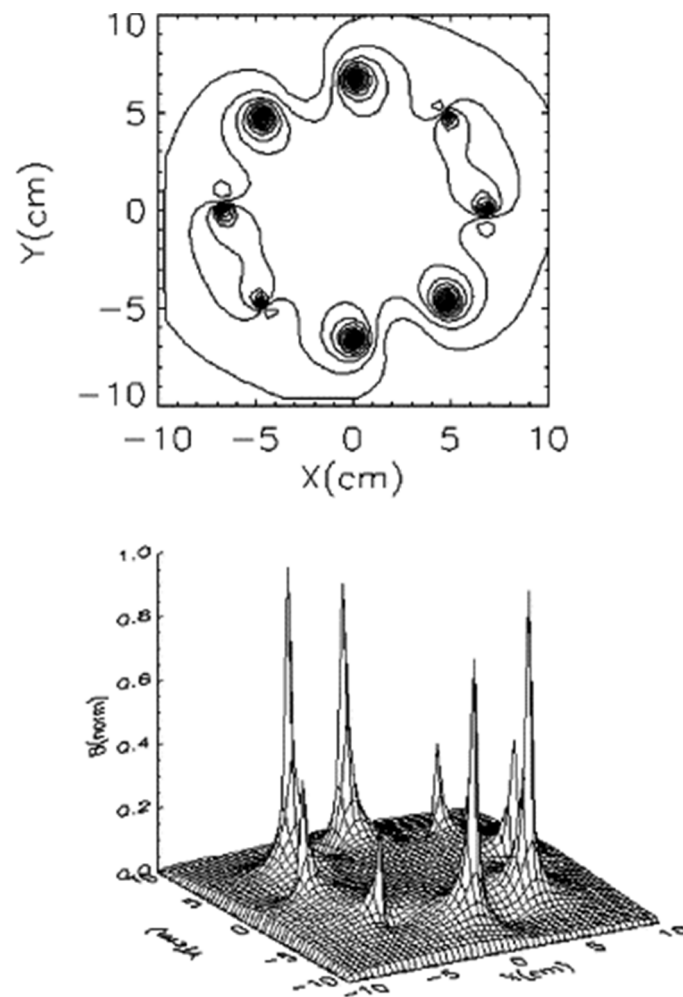


**Figure 3.**  $B_1$  field contour and three-dimensional plots of an eight-leg low-pass birdcage coil for mode 1. Reprinted from [34].

Giovannetti et al. [35] proposed a quadrature low-pass birdcage coil for operating in a vertical-bore MRI scanner, producing two  $B_1$  field components perpendicular to the vertical  $B_0$  field by exploiting the specific pattern of the current in the birdcage conductors. The quadrature detection, which provides a maximum SNR improvement of  $\sqrt{2}$ , was obtained using the dominant sinusoidal mode, producing a radial magnetic field, and a second mode generated by the coil end-rings made resonant with the addition of a capacitor on each ring able to generate a  $B_1$  field along the coil longitudinal axis, with both fields perpendicular to each other and to the  $B_0$  field [36]. The quadrature birdcage coil was then tuned at 7.66 MHz for being employed as a receive-only coil for experiments in a vertical- $B_0$  MRI system dedicated to musculoskeletal limb imaging (E-Scan 0.18T, Esaote Biomedica). Moreover, a resonant blocking circuit using crossed diodes and inductances was added for decoupling with the transmit coil. A pick-up rectangular loop was coupled to a birdcage single mesh in order to detect the  $B_1$  field produced by the fundamental mode, while the extraction of the end-ring coil mode was performed with direct coupling. Finally, the signals emitted by the coils were transferred to low-noise preamplifiers for preserving the experiment SNR (Figure 4).

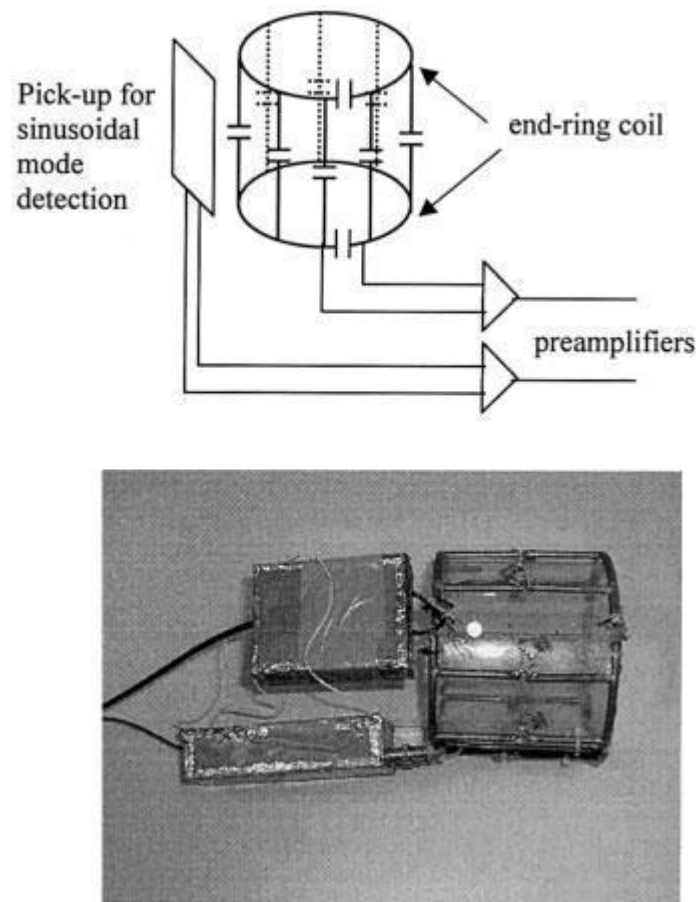


**Figure 4.** Representative sketch (**top**) and picture of the built quadrature coil (**bottom**). Reprinted from [35].

The MRI results demonstrated that such a quadrature coil configuration improved the field homogeneity along the longitudinal plane (demonstrating a 35% increase compared to the same linear birdcage coil) and provided a higher SNR (18% and 23% increases for transverse and longitudinal planes, respectively, with respect to the linear coil).

The performance of a commercial, two-channel coil suitable for knee imaging with a commercial 0.5T MR scanner (MROpen, Paramed Medical Systems srl, Italy) was analyzed with workbench tests and an FDTD simulation in Hartwig et al. [37]. The coil was constituted by two separate, geometrically decoupled elements: a four-turn solenoid and a three-loop superficial coil. Simulations were performed with the commercially available software XFDTD (Remcom, State College, PA, USA). The coil was simulated in a loaded condition by using two different loads: a homogeneous cylindrical phantom (electrical conductivity = 0.6 S/m, relative permittivity = 80) and a human voxel model, composed of a volumetric model of an adult man (age 39, height 180 cm, weight 90 kg), based on the scans from the National Library of Medicine's Visible Human Male project (Figure 5). The simulated, sample-induced resistance was compared with the resistance measured at the workbench by providing a relative error below 5% and 12.5% for the cylindrical phantom and human models, respectively. The resultant  $B_1$  field distributions estimated with the simulation were very similar to the ones directly obtained from real images [38]. Such results demonstrated the ability of the FDTD method to estimate the performance of a complex geometry for low-field MRI applications in terms of  $R_{\text{sample}}$  and sensitivity.

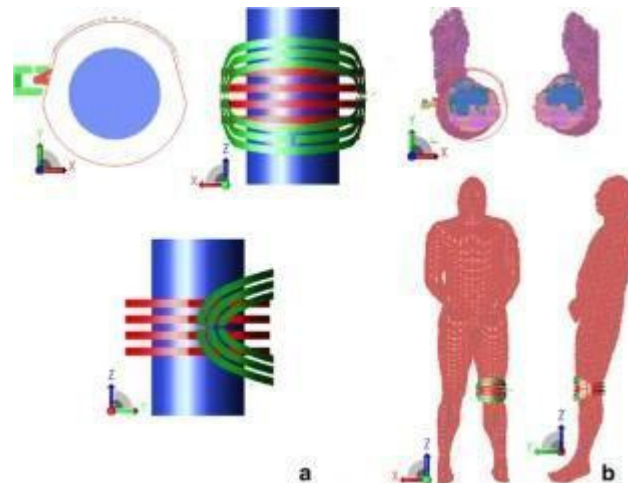


**Figure 5.** Knee coil in different loaded conditions: (a) homogenous cylindrical phantom and (b) human model. Reprinted from [37].

A successive paper investigated how the sample position affects the value of the sample-induced resistance and the decoupling between elements in the same two-channel coil using the scattering parameters (S-parameters) calculation for the simulation process. FDTD simulations demonstrated that the  $R_{sample}$  increased when the sample was nearer to the coil element and that the two coil elements were completely decoupled [39]. The sample-induced resistance estimation was performed with a method employing an exponential fitting on the voltage-oscillation damping.

These results showed that such an FDTD-based electromagnetic solver can accurately estimate the adequate position of the sample inside the coil volume and permitted an optimized study of the sample-induced effect at different loading conditions.

As has been previously described, the vertical orientation of the  $B_0$  field in many low-field MR scanners means that a solenoid coil may be employed due to its axial-field orientation. Moreover, it has the advantage of high efficiency [20], with a magnetic-field strength directly proportional to the turns number and a magnetic-field uniformity strongly determined by its length [40]. The literature also describes solenoid coils formed into individual array elements [41].

### 5.3. Phased-Array Coils

Phased-array coils are characterized by a large sensitivity region (typical of volume coils) and a high SNR, usually provided by surface coils. In their simplest design, phased-array coils consist of an array of circular or rectangular loops of copper.

Hartwig et al. [42] employed the FDTD method using the XFDTD software for evaluating coupling and shielding in phased-array coils for a 0.5 T MRI. In particular, an array constituted by two circular coils (with a radius of 5.25 cm) was simulated by automatically varying the relative distance between the center of the two elements in order to optimize the decoupling between them. Subsequently, a novel, two-element volume coil for a spine MRI, which was constituted by two identical surface elements intended to fit around the body parts to be imaged, was analyzed using FDTD (starting from the CAD project provided by the coil manufacturer) to evaluate the decoupling between the two channels and to determine the magnetic field pattern. The contribution of the shielding system was also taken into account in the simulations for evaluating its influence on the channels' decoupling and on the distribution of the magnetic field. For the two-circular-loops array, the shielding system consisted of two perfect electric conductor (PEC) rectangular plates placed parallel to the coil plane and equidistant from it while, for the volume array, the shield was constituted by two circular PEC sheets located at the structure center. Workbench tests performed on two array coils identical to the simulated one confirmed the results of the

simulations. In particular, for the unshielded array consisting of two circular loops, the geometric decoupling between elements was achieved by keeping the distance between their centers equal to 75% of their diameter. The presence of the shield induced a greater decoupling between the two array elements and simultaneously decreased the relative distance between the loop centers, providing the geometric decoupling.

Experimental results performed on the two-element volume coil for spinal column imaging with an open 0.5 T scanner (MROpen, Paramed srl, Genova, Italy) confirmed the full-wave simulation results in terms of elements decoupling and magnetic field pattern (Figure 6).

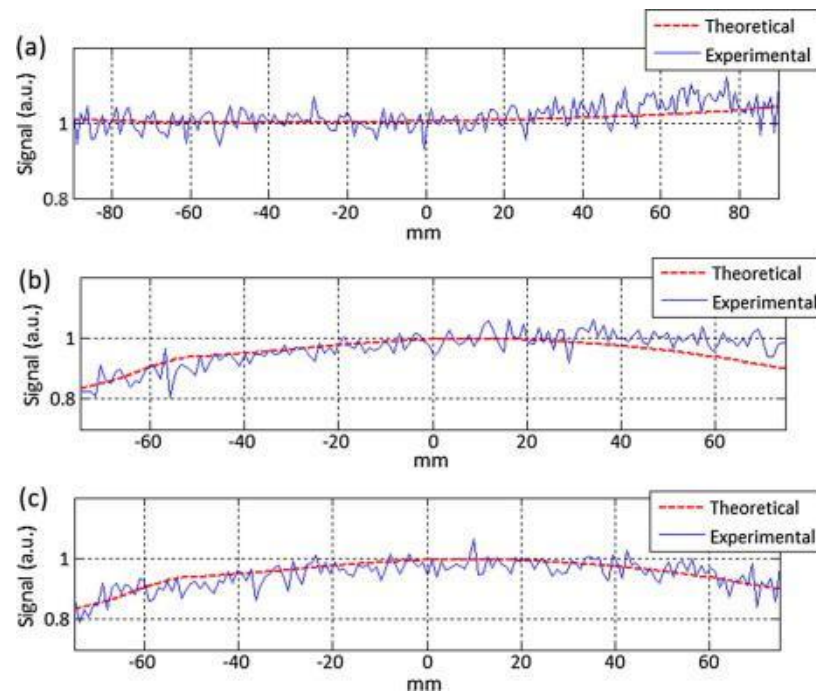


**Figure 6.** Spine volume-coil signal profiles extracted from MR images and full-wave simulations: (a) axial, (b) coronal, and (c) sagittal view. Reprinted from [42].

In particular, the presence of the shielding system did not significantly alter the decoupling between coil elements but determined a magnetic field intensity decrease while still preserving the homogeneity. Finally, the coil was used for the acquisitions of a volunteer's spine (male, 45 years old, height: 185 cm, weight: 90 kg) with a spin-echo sequence (TE = 120 ms, TR = 3175 ms, FOV  $30 \times 30 \text{ cm}^2$ , matrix  $256 \times 192$ , slice thickness 4 mm, echo number 1, spacing between slices 5 mm, number of averages 1), showing its potential for providing high-quality images (Figure 7).

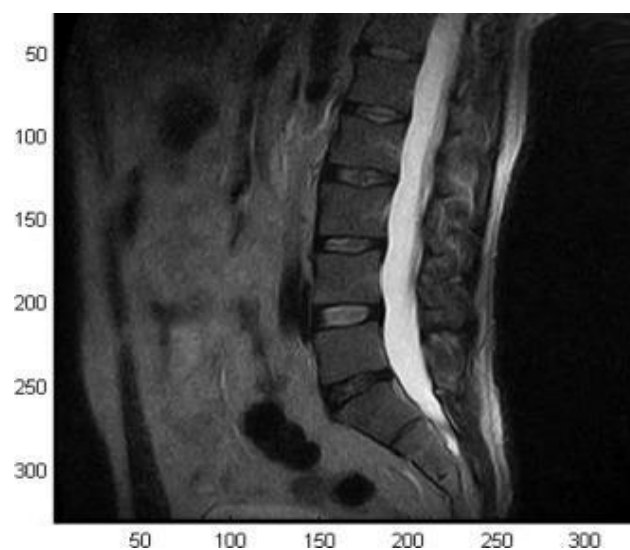


**Figure 7.** MR image of the spinal column of a volunteer (sagittal view) acquired with the spine volume coil. Reprinted from [42].

Giovannetti et al. [43] proposed an algorithm based on magnetostatic analysis for a fast calculation of the mutual inductances between array-coil elements as well as their magnetic-field patterns by taking into account the coil-conductor geometry (strip and wire). The developed software was based on IDL 6.0, and such coils were constituted by circular and square elements. Moreover, a novel array structure composed of two butterfly elements was designed and tested with electronic instrumentation. By producing a transverse RF field in the central region of the coil, this coil configuration was specifically designed for vertical  $B_0$  MRI systems (e.g., open magnets).

The simulation results of the circular- and square-loop arrays confirmed the empirically decoupled method described in the literature, in which the separation distance between the coil elements was reported to be 75% of the loop diameter and 90% of the side dimension for the circular and square arrays, respectively. The simulation results of the butterfly-elements array permitted the design of a coil providing high homogeneity when maximum decoupling of the array elements is achieved. A prototype of the butterfly-coil array was successively tested with the network analyzer HP 3577A (Hewlett Packard) for measuring the decoupling between the two elements at a frequency of 10.1 MHz (i.e., the working frequency of a 0.25 T vertical field MR scanner). The good agreement between the measured and simulated data verified the simulator accuracy.

Giovannetti et al. [44] proposed the use of a full-wave solver based on FDTD to optimize the overlap distance between the two elliptical loops of a phased-array coil (18.5 cm major axis and 10 cm minor axis), whose geometry could be useful for MRI of more elongated anatomical structures/districts. Such a coil was designed for the spine imaging of small animals in a low-field vertical MRI scanner (Esaote E-Scan 0.18 T, open MRI dedicated to musculoskeletal limb imaging).

The simulations were performed at 8 MHz with the CFDTD software package (Pennsylvania State University) by varying the overlap region between the two loops to plot the mutual coupling pattern and to calculate the position of the two elliptical elements that minimize the mutual inductance. Such simulations were conducted for both the unloaded coils and by inserting a load constituted by a parallelepiped phantom whose dielectric properties meet the ASTM criteria for MR phantom development ( $\epsilon_r = 80$ ,  $\sigma = 0.6$  S/m). Subsequently, an array prototype was built using a 2 mm diameter copper wire and three loops for each coil element in order to increase the array-coil sensitivity to loading. Moreover, since the elliptical array coil was designed as a receive-only coil, a resonant blocking circuit using crossed diodes and inductances was added to minimize the interactions between the transmitter and receiver coils. Workbench tests confirmed that

the position which minimized the mutual coupling between the two elliptical loops was identical to the one indicated by the simulation result. A quality factor of 350 and an  $r$  ratio of 3.76 were then measured. Such a designed array coil was finally employed for MRI acquisitions and was compared to a state-of-the-art commercial coil produced by Esaote for low-field shoulder imaging (Figure 8). The comparison underlined the very promising results obtained with the novel, prototype array coil, although further work was required for full optimization.



**Figure 8.** The MR experimental set-up. Reprinted from [44].

Such a planar-version prototype was followed by an elliptical array coil in a “folding” version around the small animal spine curvature, as is shown in Figure 9 [45]. The coil curvature was chosen for accommodating the animal while, at the same time, ensuring a wide FOV with a good penetration depth. After the insertion of the two elements (18.5 cm major axis, 10 cm minor axis, and 10 cm curvature radius) in the previously cited FDTD tool interface, the decoupling between them was achieved by measuring the  $S_{21}$  parameter (forward transmission gain) when varying the overlap region in order to estimate the distance between elements that minimized the mutual inductance. Such simulations, conducted at 7.67 MHz (corresponding to  $^1\text{H}$  frequency at 0.18 T), were performed successively with the unloaded coils by using a load constituted by a cylindrical phantom ( $\epsilon_r = 80$ ,  $\sigma = 0.6 \text{ S/m}$ ). The mutual-inductance plots showed that the maximum decoupling between coil elements was achieved with an inter-center distance of 7.5 cm and 6 cm for the unloaded and loaded coils, respectively. Such a difference in the coil-elements position for the loaded and unloaded array demonstrated that the knowledge of a sample-coil interaction model is very useful, not only at high frequencies but even for the design of low-frequency-tuned MRI coils.

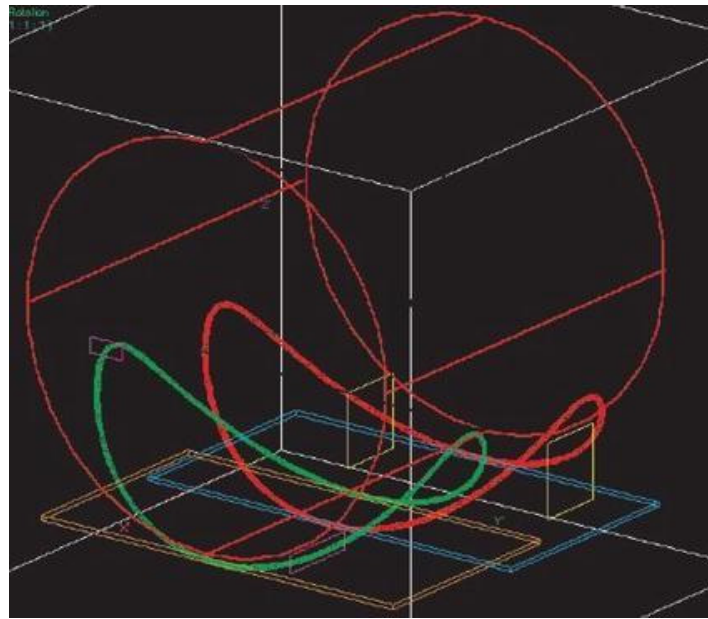


**Figure 9.** The designed two elliptical loops array. Reprinted from the [45].

The incorporation of multiple receive arrays both for higher SNRs and the reduced imaging time using parallel-imaging techniques can be useful even for low-field MR scanners. In many cases, the basic geometry is constituted by a combination of loops and butterfly coils, such as the four-element array described in [46], and is designed for thorax imaging at 0.25 T. Such array dimensions were designed for minimizing the geometry factor ( $g$ -factor) for parallel imaging with a SENSE factor of four.

## 6. Discussion

Low-field MRI has received increasing attention since low-field MR images have been shown to be diagnostically equivalent to 1.5 T images for specific applications [47]. Bandettini et al. [48] demonstrated that, by using a high-performance 0.55 T cardiovascular MRI system, it is possible to obtain good image quality, cardiac function, and quantification of volume compared to a standard 1.5 T scanner (Figure 10).

MRI systems with low field strength offer several important benefits for clinical imaging, such as the reduction of chemical shift and magnetic-susceptibility-related artifacts and the increase of T1-contrast due to the shorter T1 times [4]. In addition, the lower dielectric effects improve noise and field homogeneity. The use of low-field systems also shows several advantages for patients, such as improved comfort and low-acoustic-noise levels during scanning. Moreover, the quadratic lowering of high-frequency exposure (SAR) combined with the reduced sensitivity to metallic implants and the lower displacement forces and torques of metallic objects, leads to better patient safety and reduces the risks associated with MRI scanning in the presence of implanted metallic devices.

Our group believes that low-field MRI can make great steps in clinical relevance due to its advances in high-performance gradients and magnet technology and the development of customized RF coils.

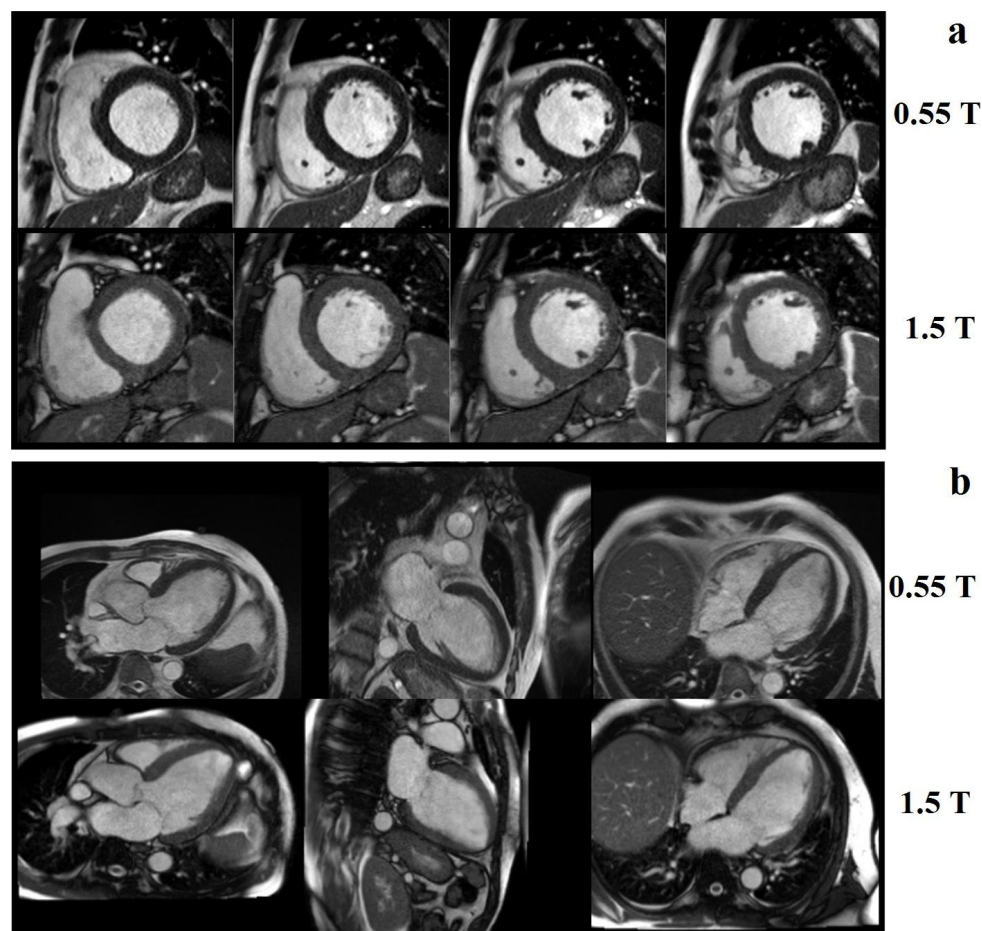


**Figure 10.** Examples of image quality at 0.55 T and 1.5 T breath-held, cine-steady, state-free precession: (a) short axis and (b) long axis slices from a patient with a nonischemic cardiomyopathy. Reprinted from [48].

In particular, recent developments in coil technology for image–SNR maximization could be applied in low-field MR scanners. For example, it is well-known that in conventional scanners the voltage induced in the receiver coil is then amplified by an amplifier and sent to the analog-to-digital converter (ADC), which performs a signal processing before the data are stored in a computer. However, cables connecting the coil to the ADC cause cross-talk and SNR reduction, especially when the channel number increases. With the use of digital coils, the MR signal analog-to-digital conversion is performed directly in the receive-coil chassis and successively transmitted to the image processor by optical fibers or wireless technology [49].

In addition, more sophisticated strategies for post-processing and image acquisition and reconstruction, such as the use of undersampling [50] or fingerprinting [51,52], will help reduce the scan time, thus increasing the clinical appeal of low-field MRI. In parallel, the increasing development and use of artificial intelligence/machine learning approaches will play a key role in overcoming some of the limitations associated with low-field MRI, such as lower SNRs and reconstruction artifacts [1]. For instance, the paper by Koonjoo et al. [53] showed the potentiality of a noise-robust deep-neural-network approach for improving the quality of low-field MR images. Artificial intelligence methods also show great promise for enhancing the diagnostic capability of MR images obtained at low field [54]. Taking into account recent technological advances, both in terms of hardware and software development, low-field MRI makes the use of MRI even more versatile for diagnostic purposes in different anatomical districts/organs. In fact, not only does low-field MRI now provide comparable performance to conventional middle- and high-field

(1.5 T) MRI for specific applications (such as cardiac [48]), but it also provides interesting attractive results for the imaging of the lungs, a conventionally critical anatomical district for MRI [55].

Given the current level of technology and the reduced operation and maintenance costs compared to middle- and high-field systems, the installation of a low-field MRI scanner may be attractive to many health care facilities, even small ones, thus leading to further deployment of MRI.

In this paper, we review the experience in our MRI laboratory focusing on the design, optimization, and testing of RF coils dedicated to MRI applications at a low magnetic field in close collaboration with MRI vendors.

The possibility to have organ-specific RF coils is extremely important, given that low-field systems have regained approval in recent years, reopening the debate on the relevance of low-field MRI in the clinical setting.

Lowering magnetic-field strength opens up new perspectives not only for cost reduction, but also for greater adaptability compared to high-field systems, widening the use of MRI to a broader range of medical applications worldwide.

The experience of our laboratory demonstrates the possibility to design, simulate, and build RF coils dedicated to low-field MR imaging of different organs. Taking into account the different loaded conditions of the coil in the simulation process, it is possible to optimize the performance of the device, thus ensuring a good image quality in terms of SNR, contrast, and achievable resolution.

For low-field scanners in particular, optimization of RF-coil performance must be performed with a careful design process, exploiting computer simulations to evaluate different coil geometries (surface-, volume-, and phased-array configurations). Subsequently, an accurate testing phase includes the measurement of coil-quality parameters with phantoms and finally with target samples within the scanner. After describing the simulation methods and quality parameters of RF coils, this paper also gives both theoretical and practical indications for an optimal low-field-scoil design in terms of choice of conductors and capacitors.

Our theoretical and experimental findings confirmed that the key issue in RF coil design is the tradeoff between achieved SNR and signal homogeneity. In particular, volume coils provide a uniform SNR across the FOV, while surface coils ensure a higher SNR near the coil which rapidly decreases with distance from the coil plane; phased arrays further increase the SNR at the same time, helping to preserve signal homogeneity.

Finally, based on the experiments conducted in our laboratory and reviewed in this paper, we believe that close collaboration between manufacturing companies and experienced laboratories/research centers offers unique opportunities in the design and optimization of RF coils dedicated to low-field MRI systems to further boost technological development in this field.

## 7. Conclusions

In this paper, we summarize the experience of our electromagnetic laboratory in developing low-field RF coils suitable for potential clinical applications in collaboration with industries. Beginning with a discussion on how RF technology can be employed to complement existing high-field devices and how low-field MRI can be made accessible to imaging where it was previously not feasible, we underline that the development of new coils provides the opportunity for lower-field-strength devices to exploit its advantages, most notably lower cost and portability.

We suppose that low-field MRI scanners will continue to develop and become more common in the future.

We believe this paper contains information useful for graduate students and researchers involved in the design of low-field MR coil and, meanwhile, could also be useful for underlying the importance of the knowledge transfer between public research institutions and industries.

**Author Contributions:** Conceptualization, G.G.; methodology, G.G.; software, G.G.; validation, G.G., F.F. and A.F.; writing—original draft preparation, G.G.; writing—review and editing, G.G., F.F. and A.F.; preparation and revision of the article, G.G., F.F. and A.F.; critical revision of the article, G.G., F.F. and A.F. All authors have read and agreed to the published version of the manuscript.

**Funding:** This research received no external funding.

**Data Availability Statement:** Not applicable.

**Conflicts of Interest:** The authors declare that they have no conflict of interest.

## References

1. Marques, J.P.; Simonis, F.F.J.; Webb, A.G. Low-field MRI: An MR physics perspective. *J. Magn. Reson. Imaging* **2019**, *49*, 1528–1542. [[CrossRef](#)]
2. Arnold, T.C.; Freeman, C.W.; Litt, B.; Stein, J.M. Low-field MRI: Clinical promise and challenges. *J. Magn. Reson. Imaging* **2022**. [[CrossRef](#)]
3. Claassen-Vujčić, T.; Borsboom, H.M.; Gaykema, H.J.; Mehlkopf, T. Transverse low-field RF coils in MRI. *Magn. Reson. Med.* **1996**, *36*, 111–116. [[CrossRef](#)]
4. Hori, M.; Hagiwara, A.; Goto, M.; Wada, A.; Aoki, S. Low-Field Magnetic Resonance Imaging: Its History and Renaissance. *Investig. Radiol.* **2021**, *56*, 669–679. [[CrossRef](#)]
5. Klein, H.M. Low-Field Magnetic Resonance Imaging. *Rofo* **2020**, *192*, 537–548. [[CrossRef](#)]
6. Guérin, B.; Villena, J.F.; Polimeridis, A.G.; Adalsteinsson, E.; Daniel, L.; White, J.K.; Wald, L.L. The ultimate signal-to-noise ratio in realistic body models. *Magn. Reson. Med.* **2017**, *78*, 1969–1980. [[CrossRef](#)]
7. Jin, J. *Electromagnetic Analysis and Design in Magnetic Resonance Imaging*; CRC: Boca Raton, FL, USA, 1999.
8. Frijia, F.; Santarelli, M.F.; Koellisch, U.; Giovannetti, G.; Lanz, T.; Flori, A. 16-Channel Surface Coil for <sup>13</sup>C-Hyperpolarized Spectroscopic Imaging of Cardiac Metabolism in Pig Heart. *J. Med. Biol. Eng.* **2016**, *36*, 53–61. [[CrossRef](#)]
9. Giovannetti, G.; Hartwig, V.; Positano, V.; Vanello, N. Radiofrequency coils for magnetic resonance applications: Theory, design, and evaluation. *Crit. Rev. Biomed. Eng.* **2014**, *42*, 109–135. [[CrossRef](#)]
10. Jin, J. *The Finite Element Method in Electromagnetics*, 3rd ed.; Wiley: Hoboken, NJ, USA, 2022.
11. Harrington, R.F. Matrix methods for field problems. *Proc. IEEE* **1967**, *55*, 136–149. [[CrossRef](#)]
12. Yee, K.S. Numerical solution of initial boundary value problems involving Maxwell's equations in isotropic media. *IEEE Trans. Antennas Propag.* **1966**, *14*, 302–307.
13. Edelstein, W.A.; Glover, G.H.; Hardy, C.J.; Redington, R.W. The intrinsic signal-to-noise ratio in NMR imaging. *Magn. Reson. Med.* **1986**, *3*, 604–618. [[CrossRef](#)]
14. Haase, A.; Odoj, F.; Von Kienlin, M.; Warnking, J.; Fidler, F.; Weisser, A. NMR probeheads for in vivo applications. *Concepts Magn. Reson.* **2000**, *12*, 361–388. [[CrossRef](#)]
15. Hoult, D.I. The principle of reciprocity in signal strength calculations—A mathematical guide. *Concepts Magn. Reson.* **2000**, *12*, 173–187. [[CrossRef](#)]
16. Hoult, D.I.; Lauterbur, P.C. The sensitivity of the zeugmatographic experiment involving human samples. *J. Magn. Reson.* **1979**, *34*, 425–433. [[CrossRef](#)]
17. Darrasse, L.; Ginefri, J.C. Perspectives with cryogenic RF probes in biomedical MRI. *Biochimie* **2003**, *85*, 915–937. [[CrossRef](#)]
18. Crozier, S.; Luescher, K.; Forbes, L.K.; Doddrell, D.M. Optimized Small-Bore, High-Pass Resonator Designs. *J. Magn. Reson. Ser. B* **1995**, *109*, 1–11. [[CrossRef](#)]
19. Hoult, D.I.; Richards, R.E. The signal-to-noise ratio of the nuclear magnetic resonance experiment. *J. Magn. Reson.* **2011**, *213*, 329–343. [[CrossRef](#)]
20. Chen, C.N.; Hoult, D.I. *Biomedical Magnetic Resonance Technology*; Adam Hilger: Bristol, UK, 1989.
21. Matick, R.E. *Transmission Lines and Communication Networks: An Introduction to Transmission Lines, High-Frequency and High-Speed Pulse Characteristics and Applications*; Wiley: Hoboken, NJ, USA, 2000.
22. Belevitch, V. Lateral skin effect in a flat conductor. *Philips Tech. Rev.* **1971**, *32*, 221–231.
23. Giovannetti, G.; Hartwig, V.; Landini, L.; Santarelli, M.F. Classical and lateral skin effect contributions estimation in strip MR coils. *Concepts Magn. Reson. Part B Magn. Reson. Eng.* **2012**, *41B*, 57–61. [[CrossRef](#)]
24. Doty, F.D.; Entzminger, G.; Hauck, C.D.; Staab, J.P. Practical aspects of birdcage coils. *J. Magn. Reson.* **1999**, *138*, 144–154. [[CrossRef](#)]
25. Giovannetti, G.; Francesconi, R.; Landini, L.; Santarelli, M.F.; Positano, V.; Viti, V.; Benassi, A. Conductor geometry and capacitor quality for performance optimization of low-frequency birdcage coils. *Concepts Magn. Reson. Part B Magn. Reson. Eng.* **2004**, *20B*, 9–16. [[CrossRef](#)]
26. Giovannetti, G.; Hartwig, V.; Landini, L.; Santarelli, M.F. Low-Field MR Coils: Comparison between Strip and Wire Conductors. *Appl. Magn. Reson.* **2010**, *39*, 391–399. [[CrossRef](#)]
27. Giovannetti, G.; De Marchi, D. Capacitors Quality Effect in Magnetic Resonance Radiofrequency Coils. *J. Med. Biol. Eng.* **2017**, *37*, 639–643. [[CrossRef](#)]

28. Giovannetti, G. Comparison between circular and square loops for low-frequency magnetic resonance applications: Theoretical performance estimation. *Concepts Magn. Reson. Part B Magn. Reson. Eng.* **2016**, *46B*, 146–155. [[CrossRef](#)]
29. Harpen, M.D. Sample noise with circular surface coils. *Med. Phys.* **1987**, *14*, 616–618. [[CrossRef](#)]
30. Giovannetti, G.; Viti, V.; Liu, Y.; Yu, W.; Mittra, R.; Landini, L.; Benassi, A. An accurate simulator for magnetic resonance coil sensitivity estimation. *Concepts Magn. Reson. Part B: Magn. Reson. Eng.* **2008**, *33B*, 209–215. [[CrossRef](#)]
31. Taylor, H.C.; Burl, M.; Hand, J.W. Experimental verification of numerically predicted electric field distributions produced by a radiofrequency coil. *Phys. Med. Biol.* **1997**, *42*, 1395–1402. [[CrossRef](#)]
32. Ma, Q.Y.; Chan, K.C.; Kacher, D.F.; Gao, E.; Chow, M.S.; Wong, K.K. Superconducting RF coils for clinical MR imaging at low field. *Acad. Radiol.* **2003**, *10*, 978–987. [[CrossRef](#)]
33. Hayes, C.E.; Edelstein, W.A.; Schenck, J.F.; Mueller, O.M.; Eash, M. An efficient, highly homogeneous radiofrequency coil for whole-body NMR imaging at 1.5 T. *J. Magn. Reson.* **1985**, *63*, 622–628. [[CrossRef](#)]
34. Giovannetti, G.; Landini, L.; Santarelli, M.F.; Positano, V. A fast and accurate simulator for the design of birdcage coils in MRI. *Magn. Reson. Mater. Phys. Biol. Med.* **2002**, *15*, 36–44. [[CrossRef](#)]
35. Giovannetti, G.; Francesconi, R.; Landini, L.; Viti, V.; Santarelli, M.F.; Positano, V.; Benassi, A. A quadrature lowpass birdcage coil for a vertical low field MRI scanner. *Concepts Magn. Reson. Part B Magn. Reson. Eng.* **2004**, *22*, 1–6. [[CrossRef](#)]
36. Hoult, D.I.; Chen, C.N.; Sank, V.J. Quadrature detection in the laboratory frame. *Magn. Reson. Med.* **1984**, *1*, 339–353. [[CrossRef](#)]
37. Hartwig, V.; Tassano, S.; Mattii, A.; Vanello, N.; Positano, V.; Santarelli, M.F. Computational Analysis of a Radiofrequency Knee Coil for Low-Field MRI Using FDTD. *Appl. Magn. Reson.* **2013**, *44*, 389–400. [[CrossRef](#)]
38. Giovannetti, G.; Viti, V.; Positano, V.; Santarelli, M.F.; Landini, L.; Benassi, A. Coil sensitivity map-based filter for phased-array image reconstruction in Magnetic Resonance Imaging. *Int. J. Biomed. Eng. Technol.* **2007**, *1*, 4–17. [[CrossRef](#)]
39. Morelli, M.S.; Hartwig, V.; Tassano, S.; Vanello, N.; Positano, V.; Santarelli, M.F. FDTD Analysis of a Radiofrequency Knee Coil for Low-Field MRI: Sample-Induced Resistance and Decoupling Evaluation. *Appl. Magn. Reson.* **2013**, *44*, 1393–1403. [[CrossRef](#)]
40. Bordelon, D.E.; Goldstein, R.C.; Nemkov, V.S.; Kumar, A.; Jackowski, J.K.; DeWeese, T.L.; Ivkov, R. Modified solenoid coil that efficiently produces high amplitude AC magnetic fields with enhanced uniformity for biomedical applications. *IEEE Trans. Magn.* **2011**, *48*, 47–52. [[CrossRef](#)]
41. Su, S.; Zou, M.X.; Murphy-Boesch, J. Solenoidal array coils. *Magn. Reson. Med.* **2002**, *47*, 794–799. [[CrossRef](#)]
42. Hartwig, V.; Vivoli, G.; Tassano, S.; Carrozzi, A.; Giovannetti, G. Decoupling and shielding numerical optimization of MRI phased-array coils. *Measurement* **2016**, *82*, 450–460. [[CrossRef](#)]
43. Giovannetti, G. Magnetostatic simulation for accurate design of low field MRI phased-array coils. *Concepts Magn. Reson. Part B Magn. Reson. Eng.* **2007**, *31*, 140–146. [[CrossRef](#)]
44. Giovannetti, G. Low field elliptical MR coil array designed by FDTD. *Concepts Magn. Reson. Part B Magn. Reson. Eng.* **2008**, *33*, 32–38. [[CrossRef](#)]
45. Giovannetti, G.; Frijia, F.; Hartwig, V.; Viti, V.; Landini, L. A Novel Magnetic Resonance Phased-Array Coil Designed with FDTD Algorithm. *Appl. Magn. Reson.* **2010**, *39*, 225–231. [[CrossRef](#)]
46. Vojtišek, L.; Frollo, I.; Valkovič, L.; Gogola, D.; Juráš, V. Phased Array Receiving Coils for Low Field Lungs MRI: Design and Optimization. *Meas. Sci. Rev.* **2011**, *11*, 61–66. [[CrossRef](#)]
47. Rutt, B.K.; Lee, D.H. The impact of field strength on image quality in MRI. *J. Magn. Reson. Imaging.* **1996**, *6*, 57–62. [[CrossRef](#)] [[PubMed](#)]
48. Bandettini, W.P.; Shanbhag, S.M.; Mancini, C.; McGuirt, D.R.; Kellman, P.; Xue, H. A comparison of cine CMR imaging at 0.55 T and 1.5 T. *J. Cardiovasc. Magn. Reson.* **2020**, *22*, 37. [[CrossRef](#)] [[PubMed](#)]
49. Serai, S.D.; Merrow, A.C.; Kline-Fath, B.M. Fetal MRI on a multi-element digital coil platform. *Pediatr. Radiol.* **2013**, *43*, 1213–1217. [[CrossRef](#)]
50. Sarracanie, M.; LaPierre, C.D.; Salameh, N.; Waddington, D.E.J.; Witzel, T.; Rosen, M.S. Low-Cost High-Performance MRI. *Sci. Rep.* **2015**, *15*, 15177. [[CrossRef](#)]
51. Mickevicius, N.J.; Kim, J.P.; Zhao, J.; Morris, Z.S.; Hurst, N.J.; Glide-Hurst, C.K. Toward magnetic resonance fingerprinting for low-field MR-guided radiation therapy. *Med. Phys.* **2021**, *48*, 6930–6940. [[CrossRef](#)]
52. Sarracanie, M. Fast Quantitative Low-Field Magnetic Resonance Imaging With OPTIMUM-Optimized Magnetic Resonance Fingerprinting Using a Stationary Steady-State Cartesian Approach and Accelerated Acquisition Schedules. *Investig. Radiol.* **2022**, *57*, 263–271. [[CrossRef](#)]
53. Koonjoo, N.; Zhu, B.; Bagnall, G.C.; Bhutto, D.; Rosen, M.S. Boosting the signal-to-noise of low-field MRI with deep learning image reconstruction. *Sci. Rep.* **2021**, *11*, 8248. [[CrossRef](#)]
54. Iglesias, J.E.; Schleicher, R.; Laguna, S.; Billot, B.; Schaefer, P.; McKaig, B. Quantitative Brain Morphometry of Portable Low-Field-Strength MRI Using Super-Resolution Machine Learning. *Radiology* **2022**, 220522. [[CrossRef](#)]
55. Heiss, R.; Tan, L.; Schmidt, S.; Regensburger, A.P.; Ewert, F.; Mammadova, D.; Buehler, A.; Vogel-Claussen, J.; Voskrebenez, A.; Rauh, M.; et al. Pulmonary Dysfunction after Pediatric COVID-19. *Radiology* **2022**, 221250. [[CrossRef](#)] [[PubMed](#)]